Latin American Journal of Solids and Structures
www.lajss.org

Failure behavior modeling of slender reinforced concrete columns subjected to eccentric load

Abstract

This work presents a numerical model to simulate the failure behavior of slender reinforced concrete columns subjected to eccentric compression loads. Due to the significant influence of the lateral displacements on the loading state provided by an eccentric load, geometric nonlinearity is considered. The responses of the concrete in tension and compression are described by two scalar damage variables that reduce, respectively, the positive and negative effective stress tensors, which lead to two different damage surfaces that control the dimension of the elastic domain. To describe the behavior of the reinforcements, truss finite elements with elastoplastic material model are employed. Interaction between the steel bars and concrete is modeled through the use of interface finite elements with high aspect ratio and a damage model designed to describe the bond-slip behavior. The results showed that the numerical model is able to represent the nonlinear behavior of slender concrete columns with good accuracy, taking into account: formation of cracks; steel yielding; crushing of the concrete in the compressive region; and interaction between rebars and concrete.

Keywords

Reinforced concrete columns: nonlinear analysis; continuum damage model; interface finite element.

E.A. Rodrigues[a]
O.L. Manzoli[b]
L.A.G. Bitencourt Jr.[a*]
P.G.C. dos Prazeres[a]
T.N. Bittencourt[a]

[a]Polytechnic School at the University of São Paulo (EPUSP), Depart. of Structural and Geotechnical Engineering, São Paulo, SP-Brazil.
[b]São Paulo State University (UNESP), Depart. of Civil Engineering, Bauru, SP-Brazil.

Corresponding author:
*luis.bitencourt@usp.br

http://dx.doi.org/10.1590/1679-78251224

Received 27.02.2014
In revised form 26.06.2014
Accepted 02.10.2014
Available online 13.10.2014

1 INTRODUCTION

Due to the important role played by reinforced concrete (RC) columns as structural elements, there are a number of papers available in the literature investigating their behavior. In most cases, the variables investigated are the slenderness ratio, concrete strength, steel ratio, boundary conditions, type of cross-section, concrete shrinkage and creep, and eccentricity loading (Kim and Yang, 1995; Claeson and Gylltoft, 1998; Diniz and Frangopol, 2003; Elwood, 2004; Majewski et al., 2008; Pallarés et al., 2008; Leite et al., 2013; Carmona et al., 2013; Bouchaboub and Samai, 2013).

After the advent of the high strength concrete (HSC) a large number of slender RC columns has been constructed, and more researchers have given special attention to this subject (Pallarés et al., 2008; Kim and Yang, 1995). Consequently, the development of numerical tools to support the analyses has increased and different numerical models to simulate the failure mechanism have been proposed. For instance, in order to investigate the behavior of RC columns under eccentric compression load, with consideration of cracks, Majewski et al. (2008) proposed an approach based on elasto-plasticity with non-local softening model. Recently, Carmona et al. (2013) developed a fracture mechanics model to describe the buckling behavior of lightly concrete columns, wherein the structural response is a result of the propagation of one single crack at the column's central region. Using the finite difference method, Bouchaboub and Samai (2013) proposed an approach to simulate the behavior of slender high strength RC columns under combined biaxial and axial compression. For all the aforementioned works, the numerical tools developed were very useful to support the nonlinear analyses and to simulate the failure mechanism presented by RC columns.

Therefore, seeking to contribute for a better understanding of the failure mechanisms of RC columns, a numerical model composed by some features which may be easily implemented in an existent finite element code is proposed. These features are made up by material models based on the Continuum Damage Mechanics Theory (CDMT) to represent the concrete and steel-concrete interface and an elastic-perfectly plastic model to simulate the steel reinforcement behavior. Moreover, the applicability of the Interface Finite Element (IFE) with very high aspect ratio proposed by Manzoli et al. (2012) is investigated for the type of problem addressed in this paper. The IFE is responsible to connect the steel rebars on the concrete matrix and, in combination with the use of an appropriate constitutive model, it is able to describe the complex bond-slip phenomenon.

Initially, to calibrate the parameters of the material models, simple compression, tension and pullout tests are carried out. After that, to assess the effectiveness of the proposed numerical approach, a number of columns subjected to eccentric compressive load are numerically analyzed. In this study, the obtained results are compared to the experimental and numerical results reported by Kim and Yang (1995); Majewski et al. (2008), respectively. The considered variables were the slenderness ratio ($\lambda = 10$, $\lambda = 60$ and $\lambda = 100$) and the concrete strength (25.5MPa , 63.5MPa and 86.2MPa) for the same steel ratio of $\rho = 1.98\%$.

This paper is organized in five main sections. In section 2 the constitutive models adopted to represent the concrete, steel reinforcements and steel-concrete interface are described. In section 3, the scheme adopted to connect the steel bars on the concrete matrix through the use of interface finite elements is presented. Later, in section 4, the features of the numerical model proposed for modeling the failure process of RC columns with different geometrical and mechanical properties are assessed. And finally, some concluding remarks are discussed in section 5.

2 CONSTITUTIVE MODELS

In this section the constitutive models adopted to represent the behavior of the materials involved in the proposed approach are described. For the concrete and interface steel-concrete, two constitutive models available in the literature based on the CDMT were implemented. For this class of models, the mechanical behavior of a damaged material is usually described by using the notion of the effective stress, together with the hypothesis of mechanical equivalence between the damage and

the undamaged material (Murakami 2012). In this paper, for the constitutive models based on the CDMT, the effective stress tensor, $\bar{\sigma}$, will assume the following form:

$$\bar{\boldsymbol{\sigma}} = \mathbf{C} : \varepsilon, \tag{1}$$

where $\mathbf{C}$ is the fourth order linear-elastic constitutive tensor, ε is the second order strain tensor and $(:)$ is the tensorial product contracted in two indices.

The reinforcement bars are modeled using the classical elastoplastic model.

2.1 A continuum isotropic damage model for concrete

To describe the nonlinear behavior of the concrete, the rate-independent version of the constitutive model based on the CDMT presented by Cervera et al. (1996) was implemented. An important feature of this model is its capability to describe different responses when subject to tensile and compression. To do this, two different scalar damage variables, d^+ and d^-, are defined for tensile and compression, respectively, which take values from zero (undamaged material) to one (fully damaged material). In addition, the effective stress tensor (equation 1) is split into tensile ($\bar{\boldsymbol{\sigma}}^-$) and compressive ($\bar{\boldsymbol{\sigma}}^+$) components, such that,

$$\bar{\boldsymbol{\sigma}} = \bar{\boldsymbol{\sigma}}^+ + \bar{\boldsymbol{\sigma}}^-. \tag{2}$$

With the aid of the above definitions, the nominal stress tensor for this model is obtained by reducing each part of the effective stress tensor, according to its respective damage variable in tension and compression,

$$\boldsymbol{\sigma} = \left(1 - d^+\right)\bar{\boldsymbol{\sigma}}^+ + \left(1 - d^-\right)\bar{\boldsymbol{\sigma}}^-. \tag{3}$$

The equivalent effective tensile and compression norms are defined by the equations 4 and 5, respectively. These positive scalar variables are used to define concepts as loading, unloading and reloading for general stress states,

$$\bar{\tau}^+ = \sqrt{\bar{\boldsymbol{\sigma}}^+ : \mathbf{C}^{-1} : \bar{\boldsymbol{\sigma}}^+}, \tag{4}$$

$$\bar{\tau}^- = \sqrt{\sqrt{3}\left(K\bar{\sigma}^-_{oct} + \bar{\tau}^-_{oct}\right)}. \tag{5}$$

The parameter $K = \sqrt{2}(\beta - 1) / (2\beta - 1)$ is a material property that depends on the relation between the uniaxial and biaxial compressive strength of the concrete, β. According Cervera et al. (1996), typical values for concrete are: $\beta = 1.16$ and $K = 0.171$. In the equation 5, $\bar{\sigma}^-_{oct}$ and $\bar{\tau}^-_{oct}$ are the octahedral normal and shear stresses, respectively, obtained from $\bar{\boldsymbol{\sigma}}^-$.

Two independent damage criteria, one for tension and other for compression, are expressed as:

$$\bar{\phi}^+\left(\bar{\tau}^+, r^+\right) = \bar{\tau}^+ - r^+ \leq 0, \text{ and} \tag{6}$$

$$\bar{\phi}^{-}\left(\bar{\tau}^{-}, r^{-}\right) = \bar{\tau}^{-} - r^{-} \leq 0, \tag{7}$$

where r^{+} and r^{-} are the current damage thresholds, which are updated continuously to control the size of the expanding damage surface. The boundary damage surfaces for the effective stresses are expressed by $\bar{\phi}^{+}(\bar{\tau}^{+}, r^{+}) = 0$ and $\bar{\phi}^{-}(\bar{\tau}^{-}, r^{-}) = 0$. At the onset of the analysis, the initial value attributed to damage thresholds are $r_0^{+} = f_t$ and $r_0^{-} = f_{c0}$, where f_t is the tensile strength and f_{c0} the compression stress threshold for damage. The evolution of the damage thresholds can be expressed in a closed form, always using the highest values reached by $\bar{\tau}^{+}$ and $\bar{\tau}^{-}$, during the loading process, i.e., $r^{+} = \max(r_0^{+}, \bar{\tau}^{+})$ and $r^{-} = \max(r_0^{-}, \bar{\tau}^{-})$.

To describe the evolution of the damage variables d^{+} and d^{-}, two exponential functions to represent the material degradation process in tension and compression are defined. These damage variables are able to determine the softening behavior in tension and the hardening/softening in compression, after reaching the initial elastic limit in tension and compression, respectively,

$$d^{+} = 1 - \frac{r_0^{+}}{r^{+}} e^{A^{+}\left(1 - \frac{r^{+}}{r_0^{+}}\right)}, \text{ and} \tag{8}$$

$$d^{-} = 1 - \frac{r_0^{-}}{r^{-}}\left(1 - A^{-}\right) - A^{-} e^{B^{-}\left(1 - \frac{r^{-}}{r_0^{-}}\right)}. \tag{9}$$

In an uniaxial tensile test, the expression shown in equation 8 is able to represent the softening in the stress-strain curve as a process degradation of quasi-brittle materials. To satisfy the mesh objectivity condition, the energy dissipated by the material in tension must to be properly related to the fracture energy of the material. Therefore, the softening parameter A^{+} is derived from the ratio between the material fracture energy and the geometric factor, l_{ch}, termed characteristic length, which corresponds to the width zone where the degradation concentrates, such that:

$$\frac{1}{A^{+}} = \frac{1}{2\bar{H}^{+}}\left(\frac{1}{l_{ch}} - \bar{H}^{+}\right) \geq 0, \tag{10}$$

where $\bar{H}^{+} = (f_t)^2 / 2EG_f^{+}$ is written in terms of the tensile strength, f_t, the elastic modulus, E, and the (tensile) fracture energy of the material, G_f^{+}. The characteristic length, depends on the spatial discretization, and in this paper, is assumed to be the square root of the finite element area.

The parameters A^{-} and B^{-} are defined so that the stress-strain curve of the concrete satisfies two previously selected points of an uniaxial experimental test.

The algorithm of the damage model described in this section was implemented as shown in Table 1. More details about the formulation can be found in Cervera et al. (1996).

2.1.1 Numerical example for validation

To illustrate the behavior of the constitutive model adopted for the concrete, uniaxial load simulations for tensile and compressive states were carried out by imposing horizontal displacement in-

crements, in a total of 100 for each branch (tension and compression). The Figure 1 shows the test setup of a fictitious concrete block numerically analyzed with a square cross section (100mm^2) discretized with two three-node triangular finite elements in plane stress condition, with an out-of-plane thickness of 100mm .

INPUT: $r_j^+, r_j^-, \boldsymbol{\varepsilon}_{j+1}$	
(1)	*Calculate* : $\overline{\boldsymbol{\sigma}}_{j+1}$
(2)	*Calculate* : $\overline{\boldsymbol{\sigma}}_{j+1}^+$ *and* $\overline{\boldsymbol{\sigma}}_{j+1}^-$
(3)	*Calculate* : $\overline{\tau}_{j+1}^+$ *and* $\overline{\tau}_{j+1}^-$
	Verify if : $\overline{\phi}^+ (\overline{\tau}_{j+1}^+, r_j^+) \leq 0$
	true : $r_{j+1}^+ = r_j^+$
	false : $r_{j+1}^+ = \overline{\tau}_{j+1}^+$
(4)	*and*
	Verify if : $\overline{\phi}^- (\overline{\tau}_{j+1}^-, r_j^-) \leq 0$
	true : $r_{j+1}^- = r_j^-$
	false : $r_{j+1}^- = \overline{\tau}_{j+1}^-$
(5)	*Calculate* : d_{j+1}^+ *and* d_{j+1}^-
(6)	*Calculate* : $\boldsymbol{\sigma}_{j+1}$
OUTPUT: $r_{j+1}^+, r_{j+1}^-, \boldsymbol{\sigma}_{j+1}$	

Table 1: Algorithm of the damage model proposed by Cervera et al. (1996).

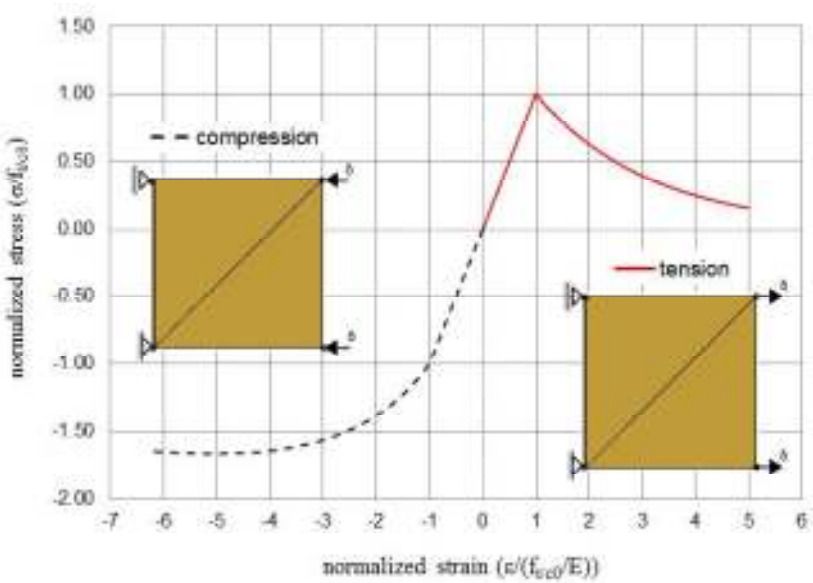


Figure 1: Normalized stress-strain curves for uniaxial tension and compression loads.

The parameters adopted in the analyses are: Young's modulus $E_c = 23.6\text{GPa}$; Poisson's ratio $\nu_c = 0.2$; fracture energy $G_f = 0.05\text{N/mm}$; tensile strength $f_t = 2.5\text{MPa}$; compression stress threshold for damage $f_{c0} = 15.0\text{MPa}$ and the compressive parameters $A^- = 1.0$ and $B^- = 0.890$.

Figure 1 shows the normalized stress versus strain curves obtained in the numerical analyses. As can be noted, for both compression and tension tests, the damage model employed is able to describe the main characteristics of the mechanical behavior of the concrete under static load.

2.2 Elastoplastic model for steel reinforcements

To simulate the behavior of the steel bars, an elastic-perfectly plastic model was employed. The Figure 2 illustrates the stress-strain relation for this model characterized by the Young's modulus E_s and the yield stress σ_y. This model is widely described in the literature and a detailed description can be found in Simó and Hughes (1998).

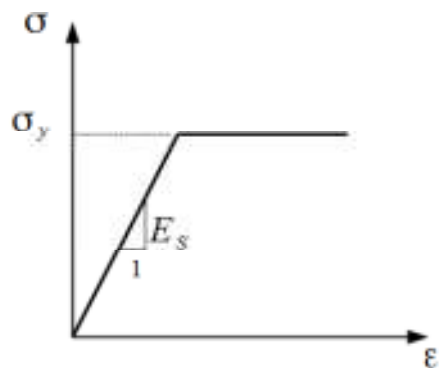


Figure 2: Constitutive model adopted for the steel bars.

2.3 J2 continuum damage model for steel-concrete interface

To represent the bond-slip behavior between the steel bars and concrete, a constitutive damage model consistent with the Continuous Strong Discontinuity Approach (CSDA) is adopted, as proposed by Manzoli et al. (2012). This model is formulated on the effective stress field associated with a scalar damage variable, $d^J \in [0,1]$, which degrades only the deviatoric part of the effective stress. Thus, the constitutive relation of the J2 damage model can be written as

$$\boldsymbol{\sigma} = \left(1 - d^J\right)\bar{\boldsymbol{S}} + \bar{\boldsymbol{\sigma}}_V, \tag{11}$$

where $\bar{\boldsymbol{S}}$ and $\bar{\boldsymbol{\sigma}}_V$ are the deviatoric and the volumetric components of the effective stress tensor (equation 1), such that:

$$\bar{\boldsymbol{\sigma}} = \bar{\boldsymbol{S}} + \bar{\boldsymbol{\sigma}}_V. \tag{12}$$

The damage criterion can be expressed in terms of the effective stress as:

$$\bar{\phi}^J\left(\bar{\tau}^J, r^J\right) = \bar{\tau}^J - r^J \leq 0, \tag{13}$$

where r^J is the current damage threshold, and $\bar{\tau}^J$ is the equivalent stress, given by:

$$\bar{\tau}^J = \frac{1}{\sqrt{2}}\left\|\bar{S}\right\|. \tag{14}$$

The evolution of the damage threshold can be expressed in a closed form, always using the highest value reached by $\bar{\tau}^J$ during the loading process, i.e., $r^J = \max(r_0^J, \bar{\tau}^J)$.

In this paper the evolution of the damage variable assumes the following form:

$$d^J = 1 - \frac{q\left(r^J\right)}{r^J}, \tag{15}$$

where $q(r^J)$ is a function (hardening/softening law) that can be calibrated from experimental tests or analytical expressions available in standard codes to describe the steel-concrete interface.

Table 2 illustrates the algorithm of the J2 damage model implemented. More details about this constitutive model can be found in Manzoli et al. (2012).

INPUT: $r_j^J, \boldsymbol{\varepsilon}_{j+1}$	
(1)	*Calculate* : $\bar{\boldsymbol{\sigma}}_{j+1}$
(2)	*Calculate* : $\bar{\boldsymbol{S}}$ *and* $\bar{\boldsymbol{\sigma}}_V$
(3)	*Calculate* : $\bar{\tau}_{j+1}^J$
(4)	*Verify if* : $\bar{\phi}^J\ (\bar{\tau}_{j+1}^J, r_j^J) \leq 0$ *true* : $r_{j+1}^J = r_j^J$ *false* : $r_{j+1}^J = \bar{\tau}_{j+1}^J$
(5)	*Calculate* : d_{j+1}^J
(6)	*Calculate* : $\boldsymbol{\sigma}_{j+1}$
OUTPUT: $r_{j+1}^J, \boldsymbol{\sigma}_{j+1}$	

Table 2: Algorithm of the J2 damage model.

3 INTERFACE FINITE ELEMENT

In the methodology applied in this work for modeling reinforced concrete columns, the interface steel-concrete is discretized using interface finite elements (IFEs), as proposed by Manzoli et al. (2012). The IFE is the standard triangular (three-node) finite element with very high aspect ratio. As described by the authors, when the aspect ratio increases (ratio of the largest to the smallest dimension), the element's strains also increase approaching the kinematics of the strong discontinuity, as in the case of the CSDA (Simó et al., 1993; Oliver et al., 1999; Oliver, 2000). Therefore, based on the same principles as those of CSDA, it can be stated that bounded stresses can be obtained from unbounded strains by means of a continuum constitutive relation, which tends toward a discrete constitutive relation as the aspect ratio increases.

The main advantages of the use of IFEs can be summarized as follows:

- it is not necessary a fine mesh in the interface steel-concrete, since the aspect ratio of this element can be very high;
- discrete constitutive relations are no longer necessary and contact elements (zero-thickness elements) or specific variational formulations are not required to introduce the effects of the cohesive stresses between elements;
- a continuum constitutive relation can be used to described the bond-slip mechanism.

Regarding the main features of the use of IFEs, it is also important to remark that:

- the matrix remains continuous and the displacement compatibility between elements is maintained;
- the IFEs overlap the concrete matrix;
- when the IFE height is much smaller than the length of the element base, only slip between the steel and concrete is allowed.

In this paper, the J2 continuum damage model described in section 2.3 is applied on the IFE to describe the bond degradation. The function $q(r)$ of equation (15) can be adjusted to reproduce any given relation law between the bond shear stress $\tau(s)$ and the interface slip s. This paper uses the interface model proposed by CEB-FIP model code 90 (1993) depicted in Figure 3. This model is expressed in terms of the parameters: $\tau_{\max}$ (maximum shear strength), τ_f (residual shear strength), s_1, s_2, s_3 and α, which depend on the concrete strength, the bar geometry (ribbed or smooth), the confining situation (confined or unconfined) and bond condition (good or poor). Thus, the hardening/softening law for this model becomes:

$$q(r) = \begin{cases} \tau_{\max}\left(\dfrac{r}{r_1}\right)^{\alpha} & \text{if} \quad q_0 < r \le r_1 \\ \tau_{\max} & \text{if} \quad r_1 < r \le r_2 \\ \tau_{\max} - \dfrac{\left(\tau_{\max} - \tau_f\right)\left(r - r_2\right)}{r_3 - r_2} & \text{if} \quad r_2 < r \le r_3 \\ \tau_f & \text{if} \quad r > r_3 \end{cases}, \tag{16}$$

with $r_i = s_i G / h$ $(i = 1,2,3)$ and $q_0 = 0$. The parameters G and h are the shear modulus and the height of the IFE, respectively.

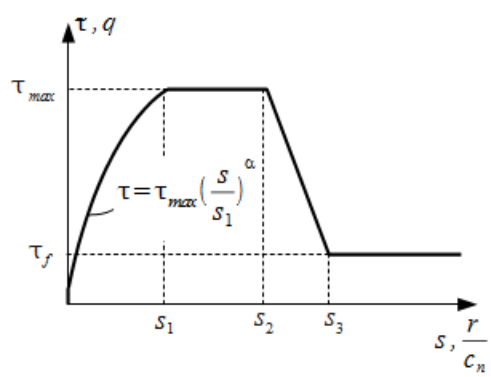


Figure 3: Interface bond-slip model for reinforced concrete CEB-FIP model code 90 (1993).

The features described above aimed to give an idea about the use of the IFE. Details about its formulation can be found in Manzoli et al. (2012).

3.1 Pullout test

In order to investigate the capability of the J2 damage model (described in the subsection 2.3) with the interface finite elements (presented in section 3) in representing the interface behavior, a pullout test with the same parameters that will be used for modeling the reinforced concrete columns is carried out.

Figure 4 shows the test setup, including the boundary conditions and finite element mesh. A steel bar of diameter $\phi_s = 10\text{mm}$ is embedded in a concrete block with a rectangular cross section of $75\text{mm} \times 100\text{mm}$. The concrete specimen is discretized with 96 three-node triangular finite elements in plane stress condition, with an out of plane thickness of 75mm. The steel bar is discretized by 6 two-node (one-dimensional) truss elements with cross-section area of $A_s = \pi\phi_s^2 / 4 = 78.54\text{mm}^2$. The bar elements are connected to the concrete elements by 6 pairs of triangular elements with thickness of $h = 1\text{mm}$ and out-of-plane thickness of $e = 31.4\text{mm}$, that corresponds to the perimeter of the cross-section of the bar in contact with the concrete. The numerical analysis has been carried out by imposing a total displacement of 2mm (in 100 steps) at the end of the bar (see Figure 4).

The concrete is assumed to be linearly elastic, with a Young's modulus of $E_c = 23.6\text{GPa}$ and a Poisson's ratio of $\nu_c = 0.2$. The steel bar is elastic-perfectly plastic, with a Young's modulus of $E_s = 210\text{GPa}$ and a yield strength of $\sigma_y = 387\text{MPa}$. For the steel-concrete interface, the hardening/softening law $q(r)$ of the J2 damage model is adjusted according to the interface model proposed by CEB-FIP model code 90 (1993). Thus, the parameters assumed here are: $\tau_{\max} = 10\text{MPa}$, $\tau_f = 1.5\text{MPa}$, $\alpha = 0.45$, $s_1 = s_2 = 0.6\text{mm}$, $s_3 = 1.0\text{mm}$ and $G = 11.8\text{GPa}$.

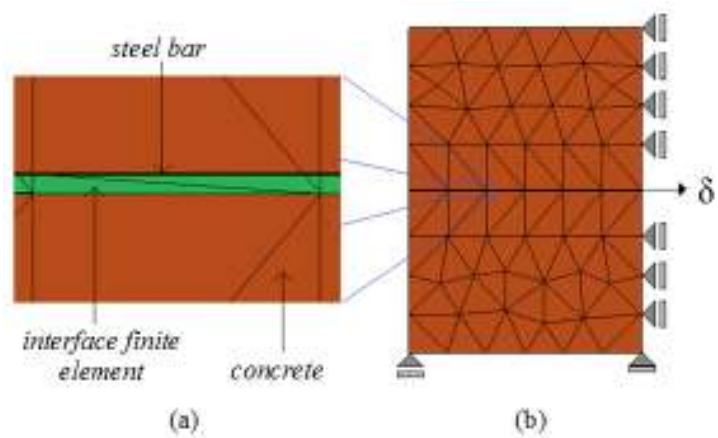


Figure 4: Pullout test: (a) detail of the interface elements; (b) geometry, finite element mesh and boundary conditions.

Figure 5 shows the average bond stress (corresponding to the ratio of the applied load to the area of the contact surface between the bar and concrete) versus imposed displacement. The different stages of the bond degradation process can be observed since the hardening /softening law of

the J2 damage model was adjusted according to the parameters of the interface model suggested by CEB-FIP model code 90 (1993). The nonlinear behavior observed in the first stage of the curve corresponds to the rebar ribs penetration into the mortar matrix phenomenon, which induces a micro cracking formation and a local crushing. This stage is represented by the expression $\tau = \tau_{\max}\left(s / s_1\right)^{\alpha}$ of the CEB-FIP model code 90 (1993), for the interval $0 \leq s \leq s_1$. The stage II illustrates the linear softening behavior of the bond stress for $s_2 \leq s \leq s_3$. Finally, the horizontal branch for $s \geq s_3$ (stage III) represents the residual bond capacity, τ_f.

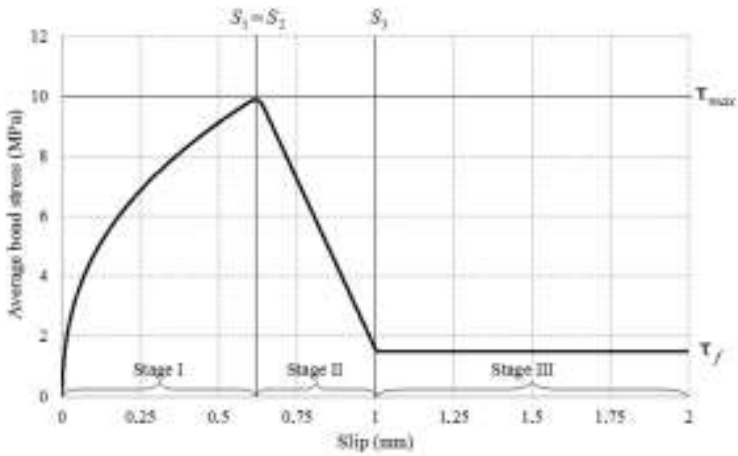


Figure 5: Bond stress-slip curve obtained with the J2 damage model.

4 NUMERICAL SIMULATIONS

4.1 Description of the columns experimentally tested by Kim and Yang (1995)

To investigate the complex behavior of reinforced concrete columns subjected to eccentric compressive load, a series of experimental tests was carried out by Kim and Yang (1995). The influences of variables like concrete strength, the slenderness ratio and the longitudinal steel ratio on the ultimate load capacity were investigated by the researchers.

A total of 30 tied reinforced columns with a square cross-section of 80mm^2 and three different heights, $L = 240\text{mm}$, $L = 1440\text{mm}$ and $L = 2400\text{mm}$ were experimentally analyzed. Consequently, three slenderness ratio were defined: $\lambda = 10$, $\lambda = 60$ and $\lambda = 100$. Moreover, three different concrete compressive strengths, 25.5MPa (normal or conventional strength concrete - NSC), 63.5MPa (middle strength concrete - MSC) and 86.2MPa (high strength concrete - HSC), and two longitudinal steel ratios of $\rho = 1.98\%$ and $\rho = 3.95\%$ were used. Figure 6 illustrates the test setup. It was considered a load eccentricity of 24mm and the rate of loading was controlled by a constant increment rate of the vertical displacement.

4.2 Finite element model

In this paper, some of the RC columns experimentally tested by Kim and Yang (1995) are numerically investigated using the ingredients of the developed methodology. Table 3 shows the geomet-

rical and mechanical properties of the nine columns analyzed with a reinforcement ratio of $\rho = 1.98\%$ and different values of the concrete strength and slenderness ratio.

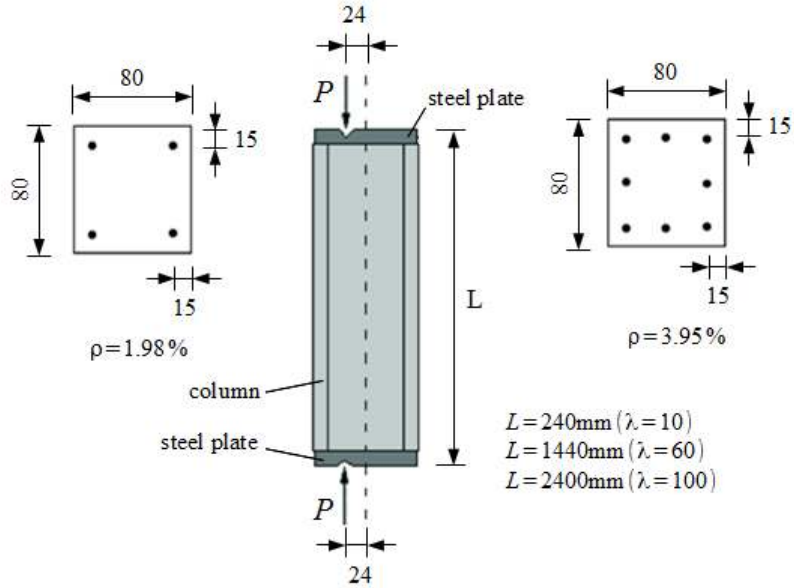


Figure 6: Geometry and boundary condition of reinforced concrete columns experimentally tested by Kim and Yang (1995).

Columns	b(mm)	h(mm)	L(mm)	f_c(MPa)	λ	ρ(%)
C1				25.5		
C2			240	63.5	10	
C3				86.2		
C4				25.5		
C5	80	80	1440	63.5	60	1.98
C6				86.2		
C7				25.5		
C8			2400	63.5	100	
C9				86.2		

Table 3: Geometrical and mechanical properties of the columns analyzed.

For all the numerical models, the same boundary conditions have been applied. Figure 7 illustrates the boundary conditions for the columns with $\lambda = 10$. An incremental vertical compression load was applied until failure. The nonlinear solution is obtained using displacement control method, in which the load process is controlled by the lateral deflection of a left-side middle point of the columns (see Figure 7).

Table 4 shows the total number of nodes and the number of each type of finite elements of the numerical analyses with slenderness ratio of $\lambda = 10$, $\lambda = 60$ and $\lambda = 100$. Three-node triangular

finite elements were used for the concrete and for the steel plates. The steel bars are represented by two-node linear finite elements (one-dimensional truss elements), which are connected to the nodes of the concrete elements by interface finite elements, as depicted in Figure 7.

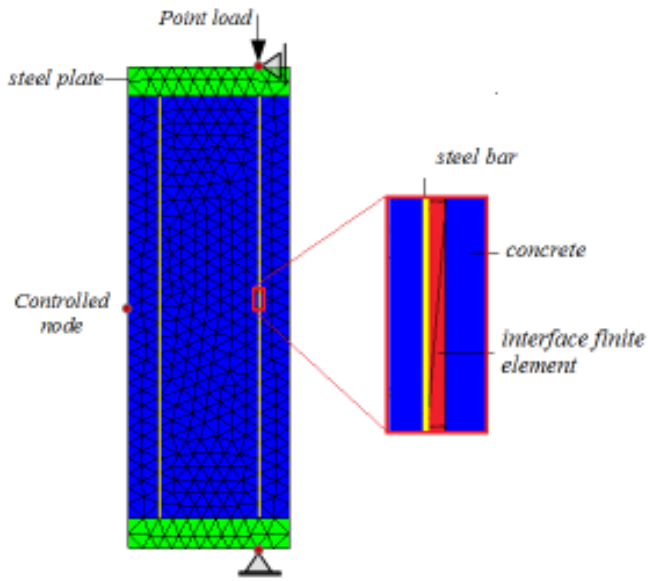


Figure 7: Numerical model built for the analysis of the columns with $\lambda = 10$.

Columns	λ	Number of truss elements	Number of triangular elements (concrete + steel plates)	Number of triangular elements for interface	Number of nodes
C1					
C2	10	56	714	112	459
C3					
C4					
C5	60	402	4892	804	3067
C6					
C7					
C8	100	678	8206	1356	5138
C9					

Table 4: Detailed data of the finite element mesh built for the numerical models.

Due to the rigid behavior of the two parallel steel plates, a linear elastic material with a high modulus of elasticity is employed. For the steel bars, the elastic-perfectly plastic material described in subsection 2.2 is assumed with Young' modulus of $E_s = 210\text{GPa}$ and yield strength of $\sigma_y = 387\text{MPa}$. The interface behavior is described by the J2 damage model described in subsection 2.3 with the same parameters employed in the pullout analysis performed in the subsection 3.1.

For the three types of concrete, NSC, MSC and HSC, the damage model proposed by Cervera et al. (1996), described in subsection 2.1 is used. The parameters employed are listed in Table 5. The

same parameters utilized to obtain the stress-strain curve shown in Figure 1 were used for the analyses of columns with NSC (C1, C4 and C7). For the columns with MSC (C2, C5 and C8) and HSC (C3, C6 and C9), the parameters as the Young's modulus and tensile strength have been calculated by the expressions suggested by Kim and Yang (1995), $E_c = 3,320\sqrt{f_c} + 6900$ and $f_t = 0.62\sqrt{f_c}$ (in MPa), respectively. Moreover, for these columns (MSC and HSC) the compression stress thresholds $r^- = f_{c0}$ were obtained by imposing that the stress-strain curve for an uniaxial compressive test (as illustrated in Figure 1) reaches the respective compressive strength for the MSC and HSC. Table 5 presents all the mechanical properties adopted for the damage model proposed by Cervera et al. (1996).

Columns	E_c(GPa)	ν	f_{c0}(MPa)	f_t(MPa)	G_f(N/mm)	β	K	A^-	B^-
C1 (NSC)	23.6		15.0	2.5					
C2 (MSC)	33.3		43.0	4.94					
C3 (HSC)	37.7		55.0	5.76					
C4 (NSC)	23.6		15.0	2.5					
C5 (MSC)	33.3	0.20	43.0	4.94	0.05	1.16	0.171	1.0	0.890
C6 (HSC)	37.7		55.0	5.76					
C7 (NSC)	23.6		15.0	2.5					
C8 (MSC)	33.3		43.0	4.94					
C9 (HSC)	37.7		55.0	5.76					

Table 5: Mechanical properties adopted for the damage model proposed by Cervera et al. (1996).

4.3 Comparison between numerical and experimental results

In this section the results obtained in the numerical simulations using the proposed methodology are compared with the experimental results obtained by Kim and Yang (1995). In addition, some results are also compared with the numerical analyses performed by Majewski et al. (2008).

4.3.1 NSC-Columns

This section presents the results obtained in the numerical simulations of the NSC-Columns with three different slenderness ratios: $\lambda = 10$ (column C1), $\lambda = 60$ (column C4) and $\lambda = 100$ (column C7), as given in Table 3.

First, the numerical results have been compared with those results obtained by Majewski et al. (2008) in terms of axial force versus axial displacement (Figure 8). Then, they also have been compared against the experimental data obtained by Kim and Yang (1995) in terms of axial force versus lateral deflection, as shown in Figure 9. It can be noted that the results obtained with the proposed methodology are in very agreement with the results available in the literature. These graphics show that the ultimate load decreases with increasing slenderness ratio.

Figures 10, 12 and 14 show the tensile damage distributions along the columns C1, C4 and C7, respectively. In turn, the compressive damage distributions are depicted in Figures 11, 13 and 15, for these same columns.

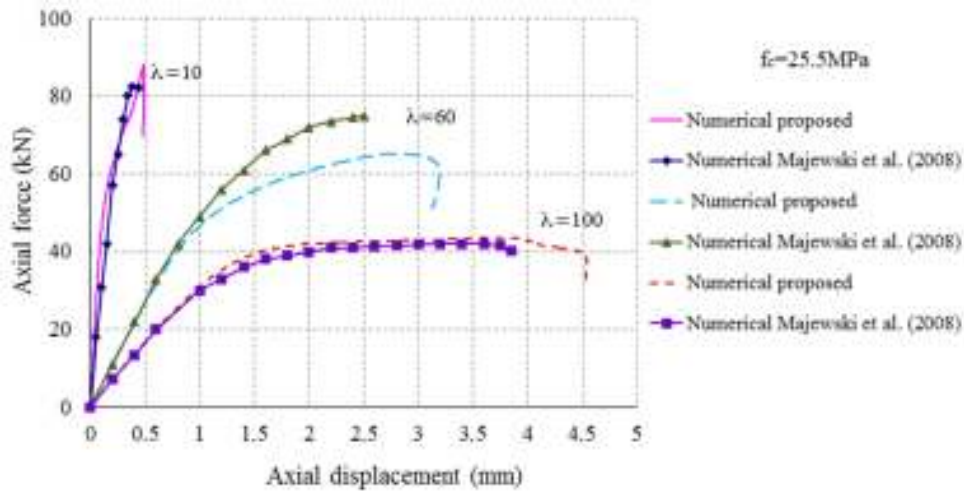


Figure 8: Axial force versus axial displacement curves for NSC-Columns.

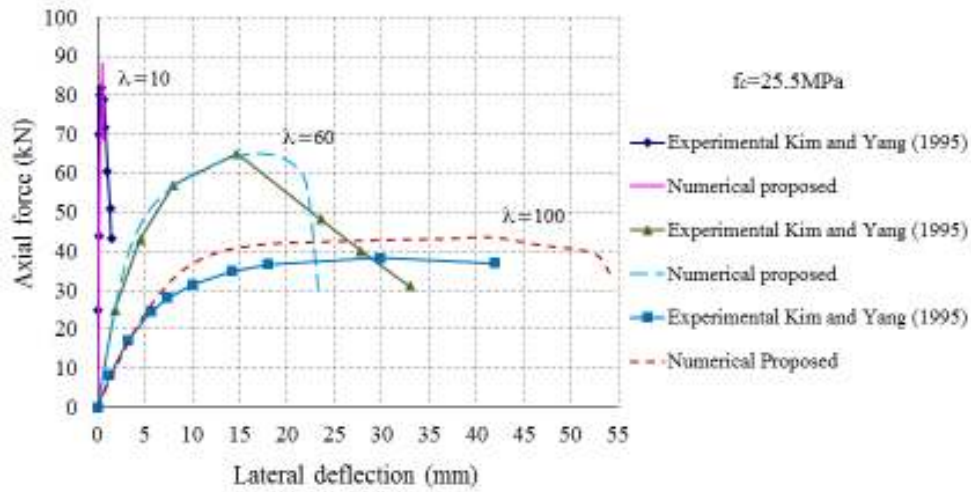


Figure 9: Axial force versus lateral deflection curves for NSC-Columns.

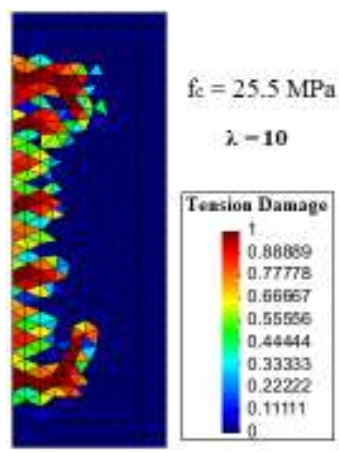


Figure 10: Tensile damage distribution for the NSC-Column with $\lambda = 10$ at the ultimate load.

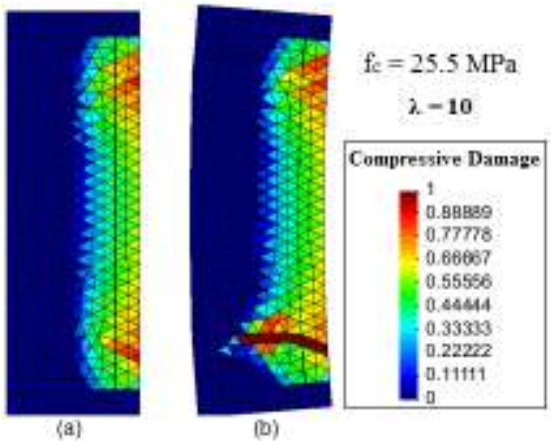


Figure 11: Compressive damage distribution for the NSC-Column with $\lambda = 10$: (a) for 70% of the ultimate load and (b) at the ultimate load.

For the column C1, with the smallest slenderness ratio, the failure process occurs by the compressive strain in concrete (Figure 11). Figures 8 and 9 show the small axial displacement and lateral deflection presented by this column.

On the other hand, for the columns C4 and C7 with the highest slenderness ratios, a large lateral and axial deflection are observed. For these cases, the failure process is driven by the increasing in tensile and compressive stress in a small region at the middle height of the columns, with a pronounced plastic yielding of the longitudinal steel bars under normal tensile stress, forming a plastic hinge mechanism or local buckling, as illustrated in Figures 12(b) and 14(b), and observed in the structural curves shown in Figures 8 and 9.

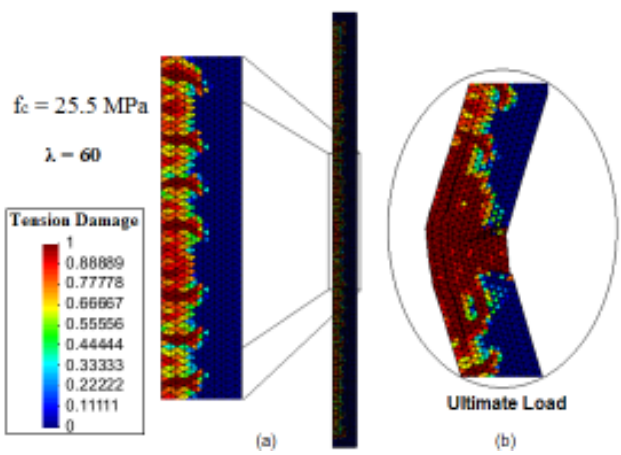


Figure 12: Tensile damage distribution for the NSC-Column with $\lambda = 60$: (a) for 70% of the ultimate load and (b) at the ultimate load.

4.3.2 MSC- and HSC-Columns

Figures 16 and 17 show the numerical results obtained for MSC-Columns and HSC-Columns, respectively, for the three different slenderness ratios considered. For both cases the results are in

good agreement with the experimental results obtained by Kim and Yang (1995). Once again, the responses show that the ultimate load decreases with increasing slenderness ratio.

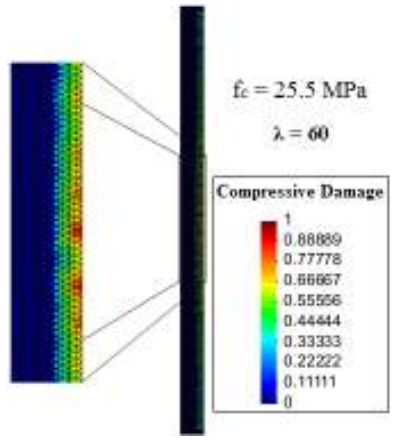


Figure 13: Compressive damage distribution for the NSC-Column with $\lambda = 60$ at the ultimate load.

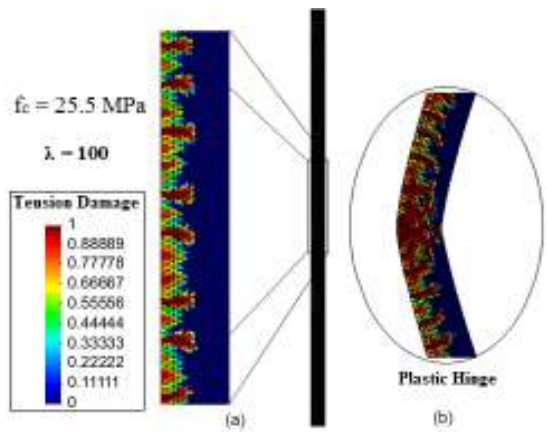


Figure 14: Tensile damage distribution for the NSC-Column with $\lambda = 100$: (a) for 70% of the ultimate load and (b) at the ultimate load.

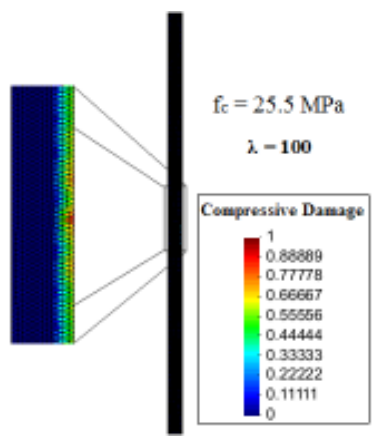


Figure 15: Compressive damage distribution for the NSC-Column with $\lambda = 100$ at the ultimate load.

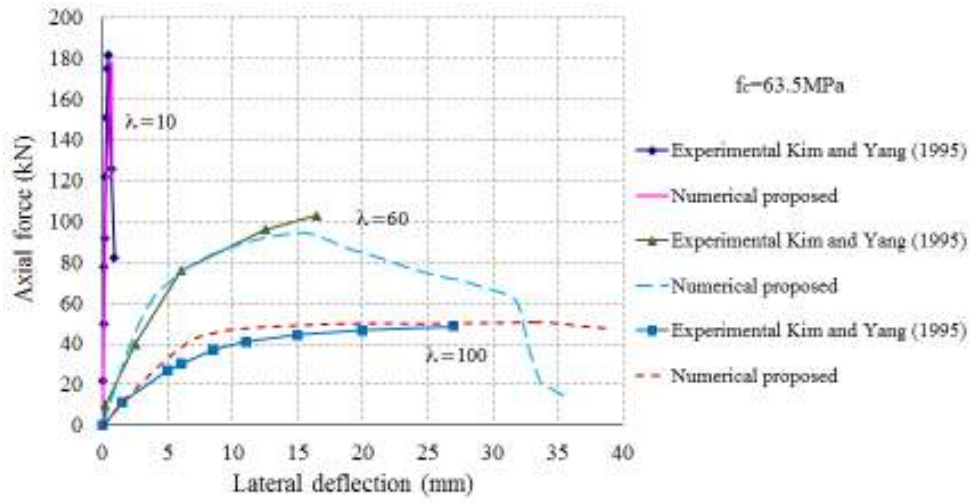


Figure 16: Axial force versus lateral deflection curves for MSC-Columns.

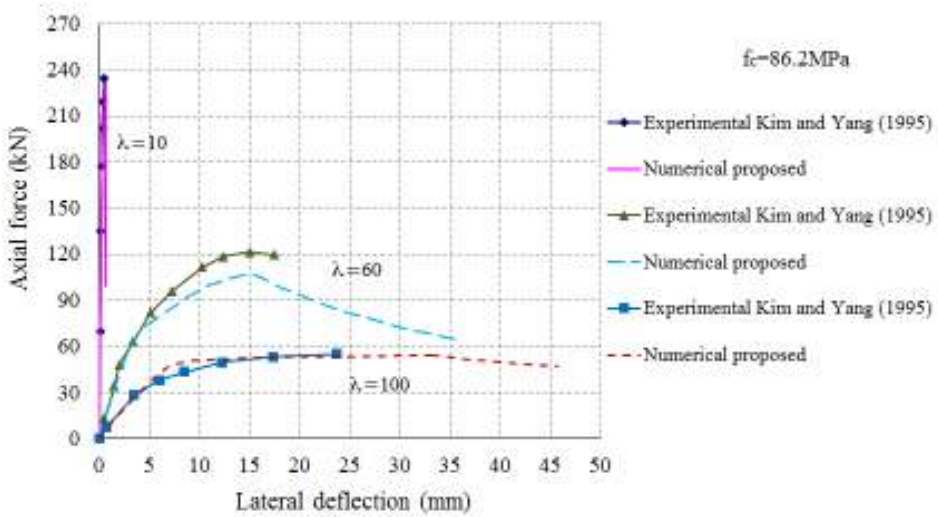


Figure 17: Axial force versus lateral deflection curves for HSC-Columns.

The tensile and compressive damage distributions for these columns can be seen from Figure 18 to 23. In general, the failure process of these columns is very similar of those obtained for the NSC-Columns, except by its magnitude. Due to the small lateral deflection presented by the columns C2 and C3 (see Figures 16 and 17), with a small slenderness ratio, the process failure of these columns is conducted by crushing of the concrete in the compressed region of the columns, as illustrated in Figure 21 for the HSC-Column.

The columns C5 and C6, C8 and C9 with slenderness ratio of $\lambda = 60$ and $\lambda = 100$, respectively, present a large lateral deflections (Figures 16 and 17). For this reason, these columns present a degradation process driven by the increase of tensile stress providing the formation, growth and coalescence of cracks, with a pronounced yielding of the tensile longitudinal steel bars, which culminates with the strain localization in a small region at the middle height of the columns, exhibiting a plastic hinge mechanism (see Figures 18(b) and 22(b)).

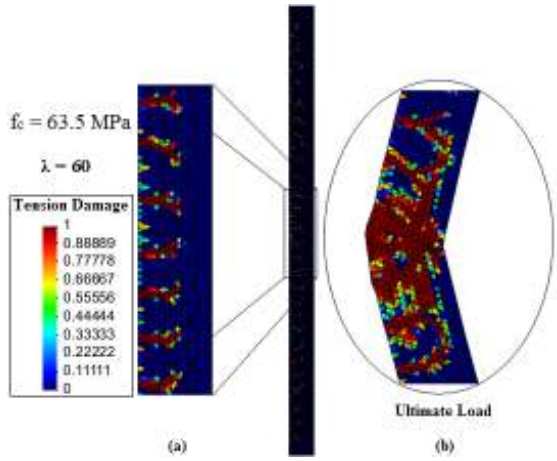


Figure 18: Tensile damage distribution for the MSC-Column with $\lambda = 60$: (a) for 70% of the ultimate load and (b) at the ultimate load.

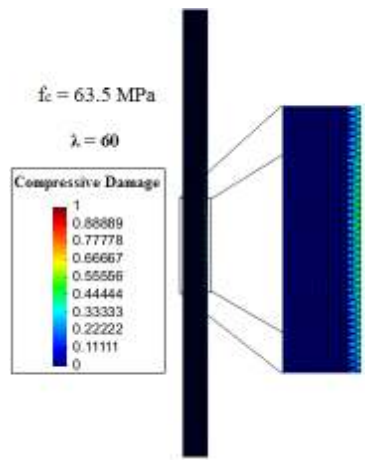


Figure 19: Compressive damage distribution for the MSC-Column with $\lambda = 60$ at the ultimate load.

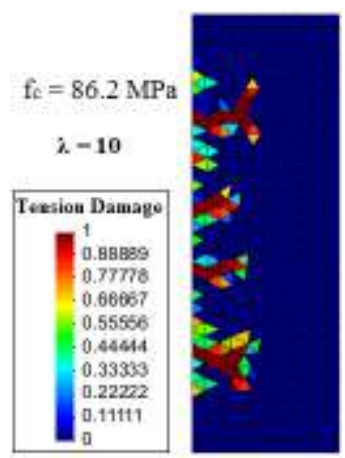


Figure 20: Tensile damage distribution for the HSC-Column with $\lambda = 10$ at the ultimate load.

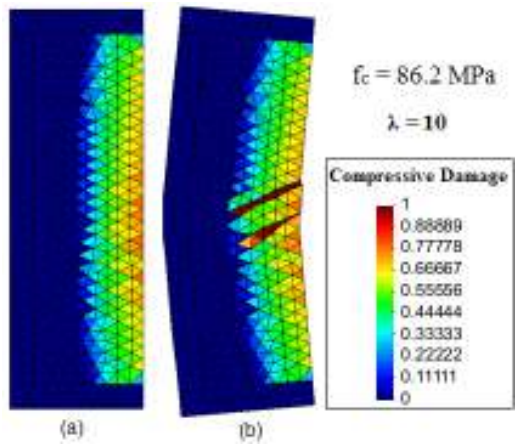


Figure 21: Compressive damage distribution for the HSC-Column with $\lambda = 10$: (a) for 70% of the ultimate load and (b) at the ultimate load.

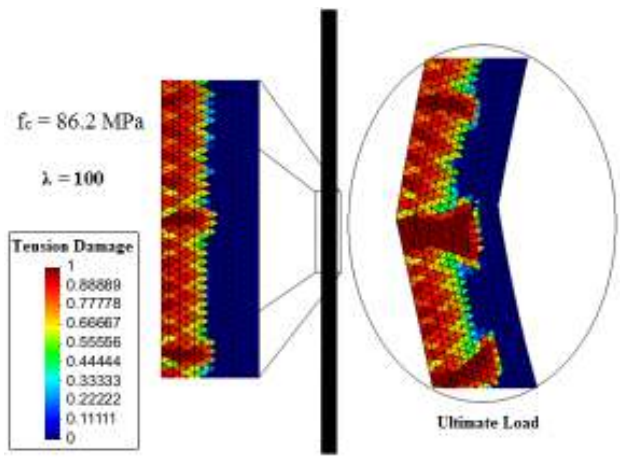


Figure 22: Tensile damage distribution for the HSC-Column with $\lambda = 100$: (a) for 70% of the ultimate load and (b) at the ultimate load.

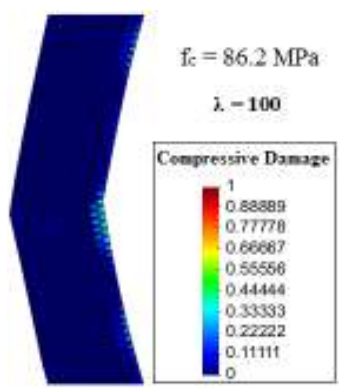


Figure 23: Compressive damage distribution (in the middle of the column) for the HSC-Column with $\lambda = 100$ at the ultimate load.

To conclude, it is also important to note that the methodology employed was able to capture the influence of the concrete strength. The results showed that for columns with slenderness ratio $\lambda = 10$, the load capacity increases, with the increasing of compressive strength. The same behavior does not occur to the columns with higher slenderness ($\lambda = 60$ and $\lambda = 100$), because the yielding of the longitudinal steel bar in tension is the factor that limits the ultimate load capacity. The curves illustrated in Figures 9, 16 and 17, for slender columns, shows that the increasing of concrete strength does not provide a significant gain in terms of the structural strength.

It should also be seen in Figures 18, 20 and 22, that the value of tensile damage is intensified in almost horizontal alignments of finite elements, from the tensioned face, with almost constant spacing. These lines of elements represent the tensile cracks, and the space between the cracks is due to the bond degradation between steel bar and concrete.

5 CONCLUSIONS

In the present work the authors sought to contribute for a better understanding of the failure behavior of reinforced concrete columns subject to eccentric compressive loads. With that purpose, a numerical approach has been proposed and its features have been implemented into an in-house finite element code. To represent the concrete behavior, the rate-independent version of the damage constitutive model proposed by Cervera et al. (1996) with different damage variables for tension and compression was implemented. Firstly, this damage constitutive model was assessed through the numerical analysis of a simple concrete block under tension and then under compression. The results showed that the damage constitutive model is able to represent the structural nonlinearity resulting from the fracture process of concrete in the tensioned region and the crushing failure of concrete in the compressed region. The complex bond-slip phenomenon on the steel-concrete interface was represented by the use of an interface finite element with very high aspect ratio and a J2 damage constitutive model, which degrades only the deviatoric part of the effective stress tensor, as described by Manzoli et al. (2012). A pullout test was performed initially to calibrate the parameters of the interface model for posterior analysis of the columns. To represent the steel bars, two-node linear finite elements (truss elements) and an elastic-perfectly plastic model, which were available in the finite element code, were used.

In the sequence, using the ingredients described above, the failure behavior of some of the columns experimentally tested by Kim and Yang (1995) were investigated. In addition, some results were also compared with those obtained numerically by Majewski et al. (2008). The variables considered in the analysis were the slenderness ratio ($\lambda = 10$, $\lambda = 60$ and $\lambda = 100$) and the concrete strength (25.5MPa, 63.5MPa and 86.2MPa) for a steel ratio of 1.98% in all the cases.

The numerical results exhibited good agreements with both, the experimental and the numerical results available in the literature, which can be confirmed by analyzing the curves obtained in terms of axial force versus axial displacement (Figure 8) and axial force versus lateral deflection (Figures 9, 16 and 17). In general, the methodology was able to reproduce the influence of the slenderness ratio and the concrete strength in the same way that was reported by Kim and Yang (1995) and by Majewski et al. (2008). The responses show that the ultimate load decreases with increasing slenderness ratio. Similar influence of the concrete strength on the failure process of NSC, MSC and HSC columns was observed. Moreover, the methodology was also able to reproduce the main fea-

tures of the failure process of the columns. Two distinct failure modes were observed. For less slender columns, the concrete plays an important role in the compression region. For them, the ultimate load occurs due to crushing of concrete. For the slender columns, the degradation process is driven by the increase of tensile stress providing the formation, growth and coalescence of cracks, with a pronounced yielding of the tensile longitudinal steel bars, which culminates with the strain localization in a small region at the middle height of the columns, exhibiting a plastic hinge mechanism.

Therefore, it is the authors' conclusion that the presented methodology is able to represent efficiently, qualitatively and quantitatively, the failure mechanism of reinforced concrete columns under eccentric compression load, reproducing efficiently the structural degradation of slender reinforced concrete columns. The main advantage obtained by the use of the methodology proposed was its easy application and calibration of the parameters of the assumed material models, including the complex interface behavior between the steel and concrete. In future investigations, the authors intend to extend the analyses for 3D problems and to consider the influence of the steel ratio in the failure process. Also, a more deep analysis about the crack pattern should be made.

Acknowledgments

This paper is a result of collaboration between researchers from the University of São Paulo (USP) and the São Paulo State University (UNESP). The authors are supported by the São Paulo Research Foundation (FAPESP) and by the National Council for Scientific and Technological Development (CNPq), for which they are gratefully acknowledged.

References

Bouchaboub, M., Samai, M.L., (2013). Nonlinear analysis of slender high-strength R/C columns under combined biaxial bending and axial compression. Engineering Structures 48: 37-42.

Carmona, J.R., Porras, R., Yu, R.C., Ruiz, G., (2013). A fracture mechanics model to describe the buckling behavior of lightly reinforced concrete columns. Engineering Structures 49: 588-599.

CEB-FIP model code 90. (1993). CEB-FIP Comitè Euro-International du Bèton, London.

Cervera, M., Oliver, J., Manzoli, O.L., (1996). A rate-dependent isotropic damage model for the seismic analysis of concrete dams. Earthquake Engineering and Structural Dynamics 25(9): 987–1010.

Claeson, C., and Gylltoft, K., (1998). Slender High-Strength Concrete Columns Subjected to Eccentric Loading. Journal of Structural Engineering, 124(3):233-240.

Diniz, S.M.C., Frangopol, D.M., (2003). Safety evaluation of slender high-strength concrete columns under sustained loads. Computers & Structures 81(14): 1475-1486.

Elwood, K.J. (2004). Modelling failures in existing reinforced concrete columns. Canadian Journal of Civil Engineering 31: 846-859.

Kim, J.-K., and Yang, J.-K., (1995). Buckling behaviour of slender high-strength concrete columns. Engineering Structures 17(1): 39-51.

Leite, L., Bonet, J.L., Pallarés, L., Miguel, P.F., Fernández Prada, M.A., (2013). Experimental research on high strength concrete slender columns subjected to compression and uniaxial bending with unequal eccentricities at the ends. Engineering Structures 48: 220–232.

Lemaitre, J., Chaboche, J.-L., (1990). Mechanics of solid materials. Cambridge University Press.

Majewski, T., Bobinski, J., Tejchman, J., (2008). FE analysis of failure behaviour of reinforced concrete columns under eccentric compression. Engineering Structures 30(2): 300-317.

Manzoli, O.L., Gamino, A.L., Rodrigues, E.A., Claro, G.K.S., (2012). Modeling of interfaces in two-dimensional problems using solid finite elements with high aspect ratio. Computers and Structures 94-95:70-82.

Murakami, S. (2012). Continuum Damage Mechanics: A Continuum Mechanics Approach to the Analysis of Damage and Fracture. Series: Solid Mechanics and Its Applications. Springer.

Oliver, J. (2000). On the discrete constitutive models induced by strong discontinuity kinematics and continuum constitutive equations. International Journal of Solids and Structures 37(48-50): 7207–7229.

Oliver, J., Cervera, M., Manzoli, O., (1999). Strong discontinuities and continuum plasticity model: The strong. discontinuity approach. International journal of plasticity 15(3): 319-351.

Pallarés, L., Bonet, J.L., Miguel, P.F., Fernández Prada, M.A., (2008). Experimental research on high strength concrete slender columns subjected to compression and biaxial bending forces. Engineering Structures 30(7): 1879-1894.

Simó, J.C., Hughes, T.J.R., (1998). Computational Inelasticity. Springer-Verlag, New York.

Simó, J.C., Oliver, J., Armero, F., (1993). An analysis of strong discontinuities induced by strain-softening in rate-independent inelastic solids. Computational Mechanics 12: 277–296.